MULTI-CYCLE LARGE EDDY SIMULATIONS IN A REALISTIC HUMAN LEFT HEART

C. Chnafa
Université Montpellier II, I3M, France.
christophe.chnafa@math.univ-montp2.fr

S. Mendez
CNRS and Université Montpellier II, I3M, France.
simon.mendez@math.univ-montp2.fr

F. Nicoud
Université Montpellier II, I3M, France.
franck.nicoud@math.univ-montp2.fr

ABSTRACT

A numerical framework designed to perform numerical simulations of the blood flow in patient-specific human hearts is presented. The heart cavities and their wall dynamics are extracted from medical images. The flow equations are written on a conformal moving computational domain, using an arbitrary Lagrangian-Eulerian approach. Additional structures (the valves) of the heart are modelled with an immersed boundary method. The resulting equations are solved numerically using a fourth-order finite-volume solver. Application of this framework on a left patient heart is presented as well. Flow dynamics is analysed in order to show the ability of the numerical procedure to reproduce the main fluid phenomena commonly observed in the left heart. The flow is characterised by its transitional nature, resulting in a complex cyclic flow. Development of weak turbulence is observed and analysed, presenting phase-averaged results.

Introduction

Today, phase-contrast magnetic resonance imaging (PC-MRI) is able to provide 3D in-vivo images of the haemodynamics in heart chambers in a non-invasive way (Markl *et al.*, 2011). Nevertheless, accuracy of the velocity field is questionable in disturbed flow (Hollnagel *et al.*, 2009). In addition, flow quantities such as wall shear stresses and pressure, which constitute relevant clinical information (Chien, 2007), cannot be measured directly with the PC-MRI method.

Computational fluid dynamics (CFD) constitutes a possible, but challenging alternative for patient-specific non-invasive flow characterisation. CFD provides data with higher spatio-temporal resolution than actual in-vivo data obtained by PC-MRI and gives the opportunity to broadly examine data sometimes inaccessible to medical imaging. The interactions between blood flow and the endocardium have been studied thanks to fluid-structure interaction (FSI) models (Tang *et al.*, 2008). However, the mechanical properties of the heart muscle, which are needed in FSI calculations, are virtually unknown and interactions of the heart with its environment have been neglected so far.

An alternative consists in using dynamic morphological medical images (4D) for the computation of the heart deformations. In this view, endocardium movements are extracted from morphological medical images and prescribed as boundary conditions of the fluid problem, thus avoiding solving the FSI problem (Midulla *et al.*, 2012). The present work describes a CFD framework based on this principle and its application to a left heart.

CFD framework

Numerical domain and fluid equations

The YALES2 solver (Moureau *et al.*, 2011*a*) used in this study is a fully explicit 3D CFD in-house code solving the unsteady, Navier-Stokes equations on unstructured grids. YALES2 was widely validated for complex engineering applications (Moureau *et al.*, 2011*b*). It is based on a spatial fourth-order finite-volume approximation. Time discretisation is performed using an explicit fourth-order Runge-Kutta scheme. Due to the transitional nature of the flow, large eddy simulations are performed using advanced subgrid scale models able to handle wall bounded flows in complex geometries (Germano *et al.*, 1991; Nicoud *et al.*, 2011). The mesh motion is handled by an Arbitrary Lagrangian-Eulerian method.

The numerical domain is extracted from 4D (3D + time) patient images. N 3D images are taken at different times $0 \leq t_0, t_1, ..., t_{N-1} < T$ during the heart cycle of period T. The choice of the starting point is of course arbitrary. Therefore, one native cardiac phase is selected at one time t_0 and the corresponding medical image is referred to as native image. The corresponding volumetric data is imported into an image processing software (ScanIP; Simpleware Ltd., Exeter, UK). The region of interest is isolated and segmentation process is made by the thresholding method (Pham *et al.*, 2000).

The three-dimensional geometric reconstruction covers all the space occupied by blood in the heart cavities. Then, the extracted geometry is imported in a commercial mesh generator (Gambit, ANSYS) to generate the grid of the native numerical domain.

Domain deformations

Fields of deformations between the native image and the others images taken at different times in the cardiac cy-

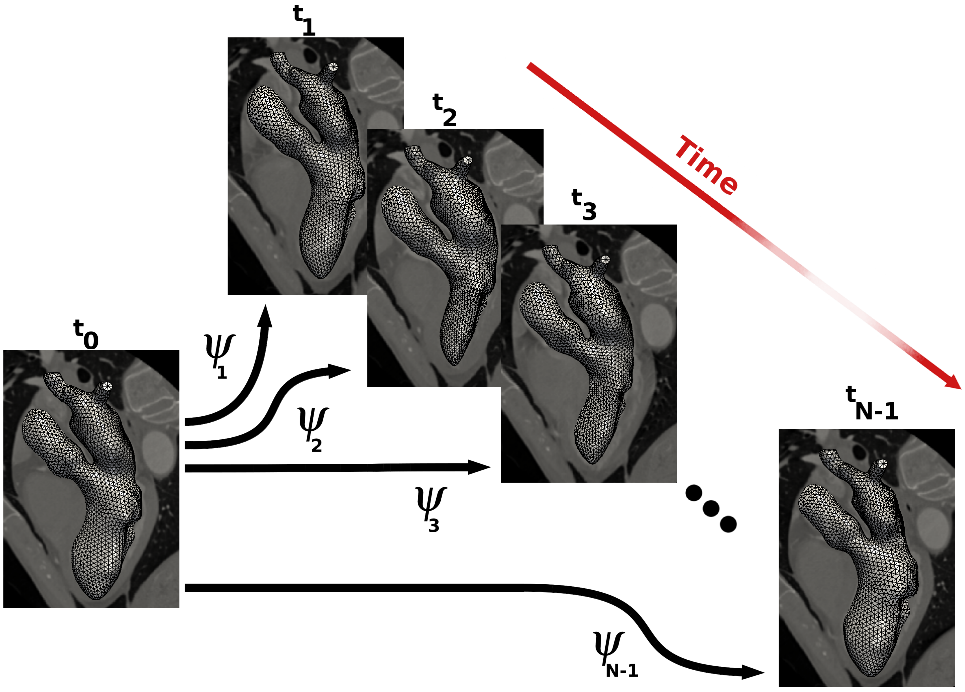

Figure 1. Mesh deformation procedure applied to a left human heart. The native mesh segmented from the image at time t_0 is deformed thanks to ψ_i to obtain the mesh at time t_i. This procedure is done for each image in the cardiac cycle in order to obtain the corresponding meshes.

cle are computed by a non-linear image registration algorithm.

The registration procedure consists in finding a transformation ψ_i which changes I_0 in I_i, viz. $\psi_i(I_0(\mathbf{x})) = I_i(\mathbf{x})$ for each $\mathbf{x}$ of each image i, where $I_i(\mathbf{x})$ stands for the pixel grey-level value of image i at position $\mathbf{x}$ in the 3D image volume Ω. The solution of this problem is of course not unique and another constraint is introduced to define ψ_i. A relevant choice is to seek for the transformation which modifies volumes as less as possible, viz. whose Jacobian is as close to unity as possible. ψ_i is then obtained from the numerical resolution of the following optimisation problem:

$$\min(F_1 + \alpha F_2) \tag{1}$$

$$F_1 = \int_\Omega \|\psi_i(I_0(\mathbf{x})) - I_i(\mathbf{x})\| \, \mathrm{d}\Omega \tag{2}$$

$$F_2 = \int_\Omega \|J(\psi_i)\| - \left\|J^{-1}(\psi_i)\right\| \, \mathrm{d}\Omega \tag{3}$$

and corresponds to the best compromise between an effective (F_1 quantity) and a simple (F_2 term) transformation. The integrals in Eq. 2 and Eq. 3 are taken over the volume Ω of the 3D image. α is a free parameter which is chosen of order unity and $\|J(\psi_i)\|$ stands for the Jacobian determinant of ψ_i (see Moreno *et al.*, 2006, for more technical details). The deformation fields ψ_i are then applied to the native mesh, producing a set of $N-1$ successive mesh phases matching the physiological cardiac images at different times as shown in Fig. 1. Surface movements are interpolated between each phase to prescribe boundary movements to the numerical domain for every time needed for the simulation. The computational mesh boundary follows the shape of the heart wall and is updated in every time step of the simulation. This principle was successfully applied to large vessels as aortas (Moreno *et al.*, 2006; Midulla *et al.*, 2012). This method enables to handle the cardiac chambers and their connected vessels. The inner grid is deformed thanks to a vertex spring method, first proposed by Batina (1989). Each segment of the grid is considered to be a spring. Motion of all internal points in the computational mesh are calculated from the prescribed boundary motion.

Other geometrical elements such as valves are out of reach of the actual 4D imaging systems. As valves are expected to have an impact on the flow structure, they must be accounted for in the simulation. The absence of precise measurement of their shape and position along the cardiac cycle makes the use of the conformal mesh method (already employed to describe the endocardium) irrelevant. In this study, both the aortic valve (AV) and the mitral valve (MV) are handled by an immersed boundary method (Mohd-Yusof, 1997). Their exact shape and dynamics are approximated using the partial information contained in the medical images. The AV which has a moderate impact on the ventricular flow is modelled as a planar region being alternatively permeable and impermeable depending on the phase in the cardiac cycle. Its location can be easily determined thanks to the aortic valve annulus, visible in the medical images. The MV is modelled by a more realistic geometry based on measurements (open surface, leaflets lengths) extracted from the medical images.

Simulation

Grid resolution and simulation details

A computed tomography (CT) exam from a patient is used to apply the numerical procedure to a healthy left heart: 10 CT-scan images are available along the cardiac cycle, which lasts 1000 ms. From the 10 images, the numerical domain and its deformations along the cardiac cycle are computed using the procedure described in the former section. As shown in Fig. 2, the domain includes the left atrium (LA), left ventricle (LV), the aortic root (AO) and the pul-

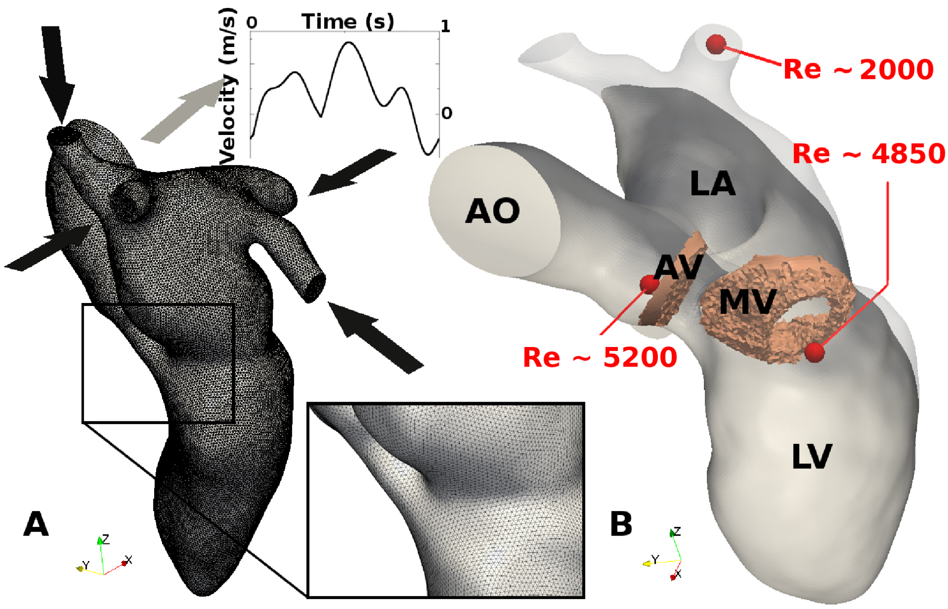

Figure 2. A: computational mesh of the luminal surface of the left heart and zoom on the grid. The inflows (pulmonary veins) are indicated by black arrows, the outflow (aorta) by the grey arrow. The inlet waveform is sketched. B: AV and MV modelled valves are visible by transparency. Peak Reynolds numbers are indicated.

monary veins. A nearly isotropic grid (Fig. 2A) is created using the commercial software ANSYS Gambit which was selected for its ability to generate good-quality tetrahedral mesh, appropriate for finite-volume formulations. The spatial resolution is imposed to be close to 0.8 mm in all three spatial directions along the cycle, which yields grids of approximately three-million tetrahedral elements.

Computational grid is deformed based on the method described in the former section. The simulation time step is fixed by a CFL condition consistent with the explicit time integration used in the CFD solver and which corresponds to a time step simulation of order of 10^{-4} s. Blood is modelled as an incompressible Newtonian fluid, of kinematic viscosity 4.10^{-6} $m^2.s^{-1}$.

The valves models can be observed in Fig. 2B, in their diastolic position (MV open, AV closed). The valves are assumed to be closed alternatively during the cardiac cycle. The time-evolution of the ventricle volume is used to separate the diastolic phase (LV volume increasing, MV open) and the systolic phase (LV volume decreasing, AV open). As either the AV or the MV is closed during the cardiac cycle, the flow waveform imposed to the four inlet conditions of the computational domain can be calculated based on the mass conservation principle. The resulting inlet velocity is periodic and varies in time during the cycle, as shown in Fig. 2A.

The information about the bulk flow characteristics at the pulmonary veins and through the MV and the AV are reported in Table 1. The inlet Reynolds number for each pulmonary vein (based on the vein diameter and the bulk velocity) varies from 0 to 2000, approximately. The Reynolds number at the mitral tips (based on the flow rate and the effective mitral mean diameter D_0, deduced from the area of the open mitral valve, A) varies from 0 to 4850, approximately. The maximum transmitral velocity, of order of 1.0 $m.s^{-1}$, falls into the usual measurements (Haugen *et al.*, 2000). The maximum Reynolds number of the aortic valve is about 5200.

Table 1. Main flow parameters describing the simulation. The maximum Reynolds number Re_{max} is calculated thanks to D_0 the diameter and the maximum flow rate at the considered element. The time when the Re_{max} is reached is reported as t_m. For the valves, A is the area of the lumen, when open.

Element	$D_0 = 2\sqrt{\frac{A}{\pi}}$	Re_{max}	t_m
AO	220 cm^2	5200	160 ms
MV	185 cm^2	4850	520 ms
Pulm. vein	100 cm^2	2000	520 ms

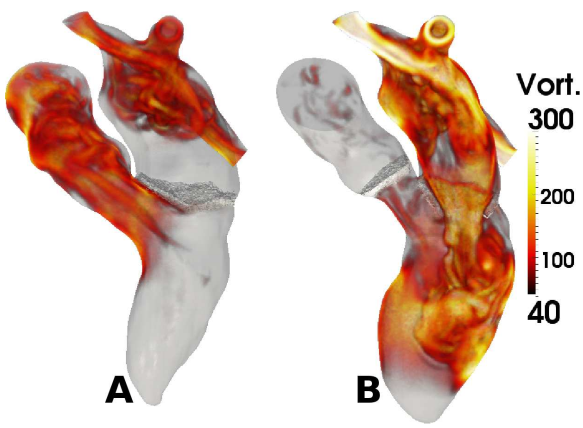

Figure 3. Vorticity magnitude in the left heart. During systole, at time t = 300 ms (A). During diastole at time t = 550 ms (B). Opacity is linked to the vorticity magnitude.

Flow overview

Figure 3 shows instantaneous three-dimensional fields of vorticity magnitude at two notable instants: the end of

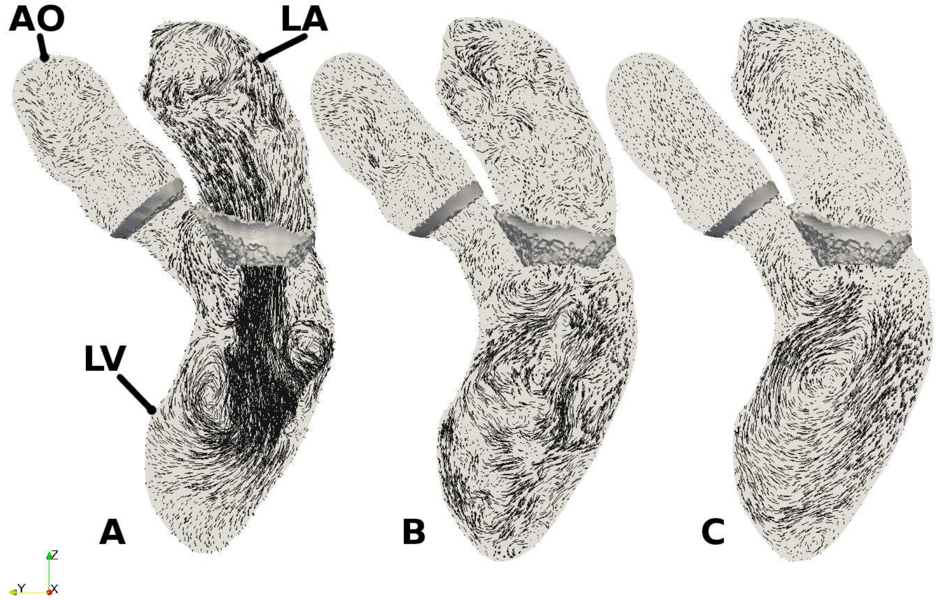

Figure 4. Slices of the left heart simulation. Velocity vectors are represented during the entering of the jet through the MV at time t = 530 ms (A) and during the late diastole phase, t = 690 ms, (B,C). (B) is an instantaneous view of the flow while (C) is the phase-averaged flow.

the systolic phase (Fig. 3A, the MV is closed, the AV open) and the beginning of the diastolic one (Fig. 3B, the MV is open, the AV closed).

During systole, the LV contracts and its volume decreases by 60%, resulting in a rapid ejection of blood to the AO. During the same phase, the LA is filled by the four pulmonary veins, forming four jets mainly deflected by each other. At the end of systole, the AV closes and the MV opens: diastole starts.

During diastole, the LV volume increases and blood passes from the LA to the LV, forming a strong jet through the MV. The jet enters the LV and is deflected along the lateral wall cavity (Fig. 3B). At this time, the inlet flow rate is maximum and blood issuing from the pulmonary veins directly flows from the top of the LA to the LV. Then, the LV volume remains quasi-constant and forms an intermediate phase called diastasis. Once diastasis is reached, a more quiescent flow is installed in the heart and is usually characterised by a recirculation cell occupying most of the LV (Markl *et al.*, 2011).

Cycle-to-cycle variations

Due to the transitional nature of this complex cyclic flow, the velocity pattern changes from one cycle to another. 20 cardiac cycles are simulated and phase averages are gathered over the last 15 cycles. Cycle-to-cycle variations are not observed during the whole cycle. During flow acceleration, the jet formed at the mitral valve is very stable (Fig. 4A). On the contrary, during phases of deceleration, transition to weak turbulence can be noted: during the late diastole, the instantaneous velocity (Fig. 4B) and phase-averaged velocity (Fig. 4C) are clearly different. While a highly disturbed flow is seen for the instantaneous view of the velocity field in the LV, a large recirculation cell and two others smaller recirculation zones are visible in the phase-averaged view. Interestingly, phase-averaged velocity flow fields are very similar to recent PC-MRI measurement of the flow in a left heart (Markl *et al.*, 2011). In the common description of the LV, the large recirculation cell is characteristic of late diastole. The present results show that this description is true only in the phase-averaged sense, while instantaneous velocity fields show that the flow is actually disorganised.

In order to investigate the cycle-to-cycle variations, turbulent kinetic energy (TKE) is analysed. The TKE is defined as

$$\mathrm{TKE} = \frac{1}{2}(u_{rms}^2 + v_{rms}^2 + w_{rms}^2) \qquad (4)$$

where u_{rms}, v_{rms}, w_{rms} denote the root mean square velocity components, in the phase-averaged sense. Note that the term 'TKE' is not perfectly adapted, as it accounts for both the turbulent fluctuations and the laminar cycle-to-cycle variations. Values of the TKE are made non-dimensional using the time-averaged inflow velocity $\overline{U}$ = 0.24 m.s^{-1}.

In Fig. 5, the spatial repartition of the TKE can be observed for two instants, t = 530 ms and t = 690 ms, corresponding to the peak diastole and late diastole, respectively. Corresponding velocity fields at the same instants are visible in Fig. 4. Before the jet impingement on the lateral wall (t = 530 ms), non-zero values of the TKE are observed only locally. Though laminar, the mitral jet shear layer exhibits small values of the TKE, showing that the jet direction is different from a cycle to another. Higher values are observed in the vortex ring marking the extremity of the jet. At t = 530 ms, the vortex ring starts impacting the wall (only part of the vortex ring interacts with the wall at that instant). The enhancement of the turbulence intensity begins as soon as the jet head hits the lateral wall because of the large velocity gradients induced by the jet-wall interaction. After its impingement on the wall, the jet disintegrates into number of small vortices. Intense fluctuations are observed near the wall (not shown). While the flow decelerates, the vortices originally located near the lateral wall move to the centre of the ventricle. As a consequence, in late diastole, maximum fluctuations are not observed near the impinging region, but

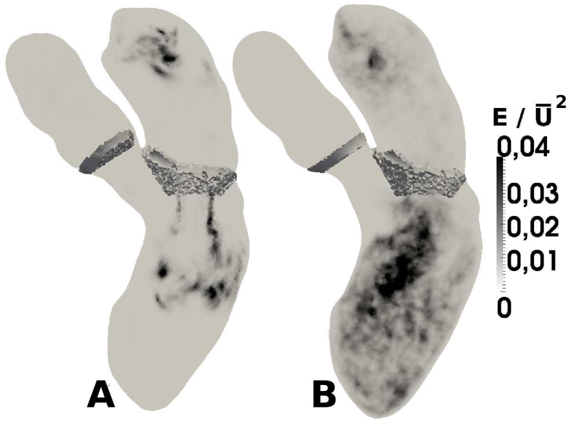

Figure 5. Field of non-dimensional turbulent kinetic energy at t = 530 ms (A), and t = 690 ms (B).

in the centre of the ventricle, as shown Fig. 5B. Maximum values of the TKE are indeed observed at the same location as the centre of the recirculating cell, displayed in Fig. 4C also at t = 690 ms. Cycle-to-cycle differences in the location of the cell centre, associated with relatively large velocity gradients in this region (see Fig. 4C) explain the high values of the TKE observed in the upper part of the LV. Velocity fluctuations are observed over most of the ventricle volume. Remarkably, the aorta root excrescence defined as the area under the aortic valve and against one of the mitral leaflet keeps turbulence-free during the diastolic period. Relatively high turbulence levels can be observed in the LA as well. The most intense turbulence takes place in the upper half region of the LA where the inflowing jets issuing from the pulmonary veins collide.

Conclusion

A numerical method developed for computations of the flow in patient-specific human hearts has been exposed and its application to a patient left heart has been described. This numerical framework only requires gated 3D images of a patient heart and global morphological parameters of the mitral valve, as input data for the computation. The numerical domain is extracted from one 3D medical image and the heart wall movements are computed from 4D medical images. A high-order numerical method is then used to solve the unsteady 3D flow equations in the reconstructed patient-specific geometry, with imposed boundary movements. The computation provides a detailed description of the blood flow dynamics in the heart.

Computation of the blood flow in one full left heart including the left ventricle, atrium and the aorta has been reported. Several simplifications were used during the course of this study in order to ease the medical images treatment. The papillary muscles were not accounted for, although they could influence the vortex breakdown during the diastole. Also, consistently with the poor time resolution of the input medical data, a rough model of the mitral valve was used, with only two possible states (open or closed). Still, the flow obtained is consistent with the current knowledge regarding the intra-cardiac blood flow, thus supporting the potential of the method. In addition, cycle-to-cycle variations are observed, thus showing that averaged information as provided by MRI only partially describes the flow structure in the left heart. Maximum cycle-to-cycle velocity fluctuations in the ventricle are observed at the end of the diastolic phase, after the impact and the breakdown of the mitral jet on the lateral wall.

REFERENCES

Batina, J.T. 1989 Unsteady airfoil solutions using unstructured dynamic meshes. *AIAA Journal* **0115**.

Chien, S. 2007 Mechanotransduction and endothelial cell homeostasis: the wisdom of the cell. *American Journal of Physiology - Heart and Circulatory Physiology* **292** (3), H1209–H1224.

Germano, M., Piomelli, U., Moin, P. & Cabot, W. H. 1991 A dynamic subgrid-scale eddy viscosity model. *Physics of Fluids* **3**, 1760–1765.

Haugen, BO, Berg, S, Brecke, KM, Samstad, SO, Slørdahl, SA, Skjærpe, T & Torp, H 2000 Velocity profiles in mitral blood flow based on three-dimensional freehand colour flow imaging acquired at high frame rate. *European Journal of Echocardiography* **1** (4), 252–256.

Hollnagel, D.I., P.E., Summers, Poulikakos, D. & Kollias, S.S. 2009 Comparative velocity investigations in cerebral arteries and aneurysms: 3D phase-contrast MR angiography, laser doppler velocimetry and computational fluid dynamics. *NMR Biomed.* **22**, 795–808.

Markl, M., Kilner, P. & Ebbers, T. 2011 Comprehensive 4D velocity mapping of the heart and great vessels by cardiovascular magnetic resonance. *Journal of Cardiovascular Magnetic Resonance* **13** (1), 7.

Midulla, M., Moreno, R., Baali, A., Chau, M., Negre-Salvayre, A., Nicoud, F., Pruvo, J.P., Haulon, S. & Rousseau, H. 2012 Haemodynamic imaging of thoracic stent-grafts by computational fluid dynamics (CFD): presentation of a patient-specific method combining magnetic resonance imaging and numerical simulations. *European Radiology* **22**, 2094–2102.

Mohd-Yusof, J 1997 for simulations of flow in complex geometries. *Annual Research Briefs-1997* p. 317.

Moreno, R., Nicoud, F., Veunac, L. & Rousseau, H. 2006 Non-linear transformation field to build moving meshes for patient specific blood flow simulations. *European Conference on Computational Fluid Dynamics* .

Moureau, V., Domingo, P. & Vervisch, L. 2011*a* Design of a massively parallel CFD code for complex geometries. *Comptes Rendus Mécanique* **339** (23), 141 – 148, high Performance Computing.

Moureau, V., Domingo, P. & Vervisch, L. 2011*b* From large-eddy simulation to direct numerical simulation of a lean premixed swirl flame: Filtered laminar flame-PDF modeling. *Combustion and Flame* **158** (7), 1340 – 1357.

Nicoud, F., Toda, H.B., O. Cabrit, S. Bose & Lee, J. 2011 Using singular values to build a subgrid-scale model for large eddy simulations. *Phys. Fluids* **23**.

Pham, D.L., Xu, C. & Prince, J.L. 2000 Current methods in medical image segmentation. *Annual Review of Biomedical Engineering* **2**, 315–337.

Tang, D., Yang, C., Geva, T. & del Nido, P. J. 2008 Patient-specific MRI-based 3D FSI RV/LV/patch models for pulmonary valve replacement surgery and patch optimization. *Journal of Biomechanical Engineering* **130** (4), 041010.